Indium antimonide photovoltaic cells for near-field thermophotovoltaics

Dilek Cakiroglu, Jean-Philippe Perez, Axel Evirgen, Christophe Lucchesi, Pierre-Olivier Chapuis, Thierry Taliercio, Eric Tournié, Rodolphe Vaillon

This manuscript is published in Solar Energy Materials and Solar Cells
https://doi.org/10.1016/j.solmat.2019.110190

Indium antimonide photovoltaic cells for near-field thermophotovoltaics

Dilek Cakiroglu[1], Jean-Philippe Perez[1], Axel Evirgen[1,*], Christophe Lucchesi[2], Pierre-Olivier Chapuis[2], Thierry Taliercio[1], Eric Tournié[1], Rodolphe Vaillon[1,2]

[1]*IES, Univ. Montpellier, CNRS, F-34000 Montpellier, France*

[2]*Univ Lyon, CNRS, INSA-Lyon, Université Claude Bernard Lyon 1, CETHIL UMR5008, F-69621, Villeurbanne, France*

** Current address: III-V Lab, Thales Research and Technology, Route départementale 128, 91767 Palaiseau, France*

Abstract – Indium antimonide photovoltaic cells are specifically designed and fabricated for use in a near-field thermophotovoltaic device demonstrator. The optimum conditions for growing the p-n junction stack of the cell by means of solid-source molecular beam epitaxy are investigated. Then processing of circular micron-sized mesa structures, including passivation of the side walls, is described. The resulting photovoltaic cells, cooled down to around 77 K in order to operate optimally, exhibit excellent performances in the dark and under far-field illumination by thermal sources in the [600-1000] °C temperature range. A short-circuit current beyond 10 μA, open-circuit voltage reaching almost 85 mV, fill factor of 0.64 and electrical power at the maximum power point larger than 0.5 μW are measured for the cell with the largest mesa diameter under the highest illumination. These results demonstrate that these photovoltaic cells will be suitable for measuring a near-field enhancement of the generated electrical power.

Keywords: thermophotovoltaics, InSb, MBE, passivation.

I. INTRODUCTION

Thermophotovoltaics (TPV) is the process by which infrared thermal radiation power is converted into electrical power using a low bandgap photovoltaic cell [1,2]. Near-field thermophotovoltaics (NF-TPV) is an extension of the same process, where benefit is taken from evanescent waves to increase by large factors the thermal radiation transfer between a hot emitter and a photovoltaic (PV) converter, and hence the electrical power generation presumably by similar factors [4-6]. Moving from principles to practice took almost two

decades: indeed, the near-field enhancement of electrical power generated by InAsSb and InAs photovoltaic cells was experimentally demonstrated very recently [7]. In this groundbreaking work, the PV cells were neither specifically designed nor fabricated in order to operate under near-field thermal irradiation conditions. The measured current-voltage characteristics were all straight lines (fill factor equal to 0.25) and the open-circuit voltages were all smaller than two millivolts.

Even though multiple theoretical analyses dealt with modelling the transport of electrical charges within the photovoltaic cell of a NF-TPV device [8-25], the steps of (1) designing, (2) fabricating and characterizing, and (3) operating a PV cell in the near field were never completed successively. The present article is about realizing the second step in that series in the case of a cell made of indium antimonide (InSb). The reasons for selecting this specific semiconductor material were given in the article describing step (1), *i.e.* the design [23]. They are briefly summarized in the following for a better understanding of the applied strategy. One important present limitation in near-field thermal radiation measurement setups is the temperature of the hot side (thermal emitter in a NF-TPV device): the largest values reached so far are 720 K (the cold side being at 460 K) in [26], and ~655 K (the cold side being at near room temperature) in [7]. With such emitter temperatures (~700 K), Wien's law tells that the bandgap should preferably be smaller than 0.28 eV to collect most of the thermally emitted photons. Narrow-bandgap (~0.2 eV at 300 K) InAs/GaSb superlattice based interband cascade structures are currently being developed for TPV applications. They have the advantage to operate at room temperature, with promising demonstrated conversion efficiencies (3.6%) in the far field, at the expense of complex heterostructures [27]. Indium antimonide, having a very low bandgap (0.17 eV at 300 K and 0.23 eV at 77 K), is also very well suited for TPV applications and a simple homojunction can be used. However, such a junction cannot operate at room temperature and must be cooled down, typically at around 77 K. Up to now, InSb photodiodes were developed for imaging applications in the mid-infrared (2-5 µm) range and not for photovoltaic power generation, in particular in the configuration where electrical carriers are photogenerated under near-field thermal irradiation conditions.

In this context, the present article is about the fabrication and characterization of a photovoltaic cell made of indium antimonide, specifically designed [23] for subsequent use in a laboratory demonstrator of a NF-TPV device. Fabrication and experimental procedures are described in section II. In particular, optimum conditions for layer growth and dopant incorporation for the active zone of the cell structure by means of Molecular Beam Epitaxy are established. Then the technological processes for passivating the side walls of micron-sized mesa-etched p-n junction diodes and putting the front and back contacts are presented in details. In section III,

electrical characterizations of the cells in the dark and under far-field illumination are discussed. Results demonstrate that the fabricated InSb cells behave as efficient diodes, and generate a photovoltaic power with short-circuit currents of several microamps and open-circuit voltages of dozens of millivolts.

II. FABRICATION AND EXPERIMENTAL PROCEDURES

II.1. MOLECULAR BEAM EPITAXY

InSb detectors are usually fabricated using standard planar methods where the p-n junction is formed by ion implantation on the front side of an InSb bulk substrate. Such methods have a deleterious effect on crystal quality. To overcome these drawbacks, molecular beam epitaxy (MBE) is of great interest since it was shown that InSb epi-diodes operating at 95 K-100 K have the same electrical performances as standard InSb planar-diodes operating at 77 K [28].
The samples were grown by solid-source MBE on Te-doped, n-type, (001) ± 0.1° oriented InSb substrates in a multi-chamber RIBER 412 reactor equipped with an antimony-valved cracker cell providing Sb_2 species. Growth rates were inferred from flux measurements carefully calibrated by reflection high-energy electron diffraction (RHEED). Growth temperature was measured with an optical pyrometer calibrated using (2x4) to (5x1) surface reconstruction transition observed on the InSb surface in static conditions [29]. Beryllium was used as the p-type dopant.

II.1.1. Oxide removal

Since the desorption temperature of In_2O_3 is close to the melting point of InSb (~527 °C), standard thermal oxide removal techniques are not appropriate for InSb. Therefore, surface oxides were removed during 30 min at low temperature (400 °C) by exposing the surface to a hydrogen overpressure (~ $2\ 10^{-5}$ Torr) using an ADDON RF plasma source. By doing so before the growth, it was ensured that the surface is smooth and the InSb wafer's temperature kept low enough [30]. At the end of the deoxidation stage, the removal of In and Sb based oxides gave rise to pseudo (1x3) surface reconstructions observed on RHEED patterns exhibiting an epi-ready InSb surface.

II.1.2. Optimum growth conditions

In order to achieve optimum MBE growth conditions of 1 µm-thick InSb test layers, two main parameters were investigated: the growth temperature (T_G) and the incorporation rate ratio

(*IRR*) defined by $IRR = R_{Sb} / R_{In}$, where R_{Sb} and R_{In} are respectively the growth rates in monolayers per second (ML/s) of indium and antimony, calibrated using RHEED oscillations. For indium, R_{In} = 0.5 ML/s was selected as a good trade-off between growth duration and crystal quality. The structural quality of the epitaxial layers was assessed using both high resolution (004) X-ray diffraction (HRXRD) and atomic force microscopy (AFM). As a result of these investigations, the optimum MBE growth conditions were found to be T_G = 440 °C and *IRR* = 4. Figure 1 (a) shows XRD spectra performed when T_G = 440 °C and *IRR* = 3 and 4. The corresponding full-widths at half-maximum (FWHM) of the diffraction peaks are respectively equal to 58 arcsec and 19 arcsec. In Fig. 1 (b), well-defined atomic steps associated with a root-mean-square (RMS) surface roughness of only 0.25 nm (less than one monolayer for Sb-based materials) are visible on a 20 x 20 µm^2 AFM image.

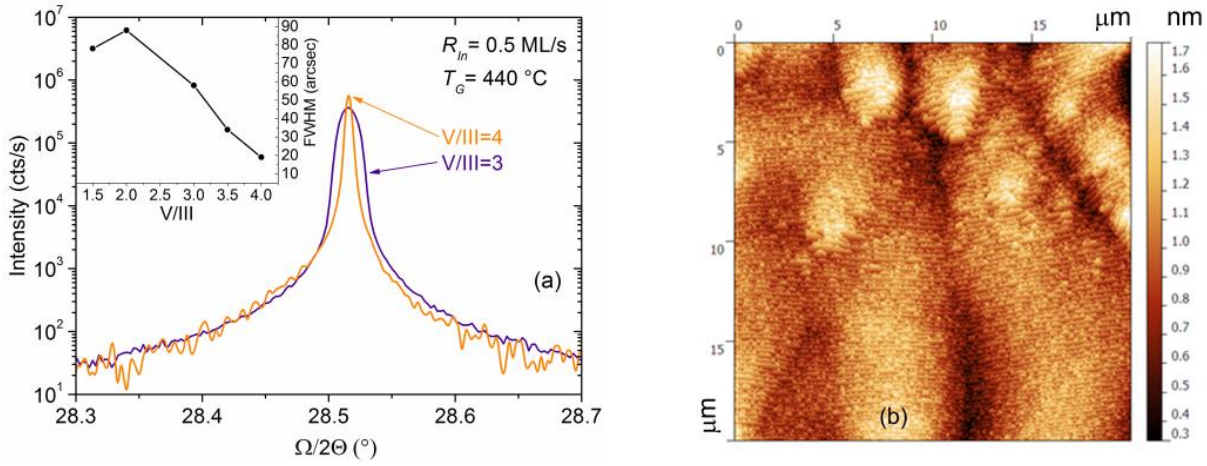

FIG. 1: (a) High-resolution XRD spectrum (004) reflection spectra of InSb layers grown by MBE with T_G = 440 °C and *IRR* = 4 or 3. Inset: FWHM of the diffraction peaks shown as a function of *IRR*. (b) 20 x 20 µm^2 AFM image when *IRR* = 4 and T_G = 440 °C.

To complete the analysis, photoluminescence (PL) measurements were performed using a Brucker Vertex 70 Fourier transform infrared (FTIR) spectrometer. When *IRR* = 4, PL spectra measurements performed at 80 K on samples grown by MBE with T_G = 370 °C or T_G = 440 °C are reported in Fig. 2. PL peaks centered at 0.234 eV (λ_P = 5.3 µm) with a typical FWHM of 20 meV correspond to the band-to-band carrier recombination. The most intense PL peak confirms that the optimum growth temperature is 440 °C.

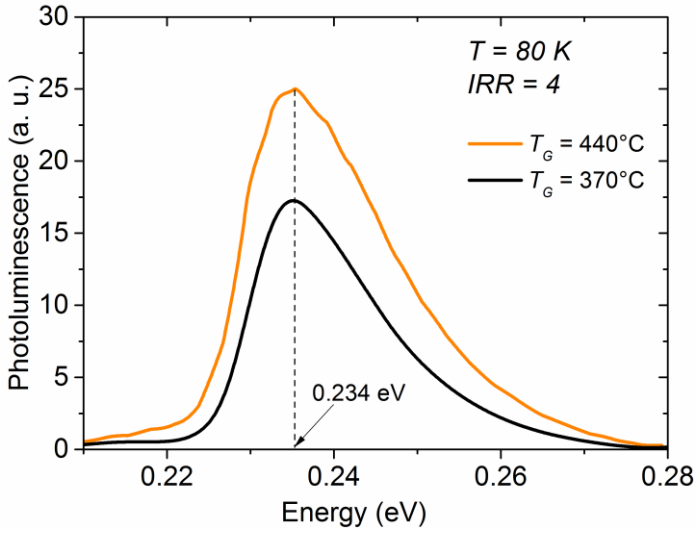

FIG. 2. Photoluminescence spectra measurements performed at $T = 80$ K for InSb layers grown by MBE with $IRR = 4$ and $T_G = 440$ °C or 370 °C.

II.1.3. Dopant incorporation

The active zone of the fabricated photovoltaic cells is a p-on-n InSb junction. p-doped and n-doped InSb layers were grown on an InSb substrate (n-doped with $N_{d,sub} = 4\ 10^{17}$ cm^{-3}). In a previous work, near-field radiation transfer and low-injection charge transport simulations were used to find the optimum architecture of the p-n junction layers in terms of their thickness and doping concentrations [23]: the top p-layer must be 0.5 µm thick with $N_a = 10^{17}$ cm^{-3} and the bottom n-doped layer must be 2.5 µm thick with $N_d = 10^{15}$ cm^{-3}.

It is worth noticing that the targeted doping concentration of the n-doped layer is very close to the background carrier concentration obtained for non-intentionally doped InSb layers. Indeed, from standard capacitance-voltage (C-V) measurements performed at a frequency of 1 MHz on different p-n junctions, doping concentrations (N_d) values ranging from $8\ 10^{14}$ cm^{-3} to 10^{15} cm^{-3} were systematically found using

$$N_d = -2\left(q\varepsilon_0\varepsilon_{\mathrm{InSb}} \frac{d\left(\frac{A}{C}\right)^2}{dV} \right)^{-1}, \qquad (1)$$

where A is the area of the mesa structure (see section II.2), V is the applied bias of the diode, q is the electron charge, ε_0 is the dielectric constant and $\varepsilon_{\mathrm{InSb}} = 15.7$ the relative dielectric constant of InSb.

In order to measure the incorporation of the Be dopant in the p-type top layer of the structure, secondary ion mass spectrometry (SIMS) measurements were made at 300 K. Prior to these

measurements, calibrations were done using reference samples of InSb with implanted Be. Then, three 500 nm-thick Be-doped layers were grown with Be effusion cell temperatures of 800 °C, 850 °C and 900 °C. For 850 °C, the corresponding SIMS profile is shown in Fig. 3 (a). A constant concentration in the doped layer and a sharp layer/substrate interface are visible. Fig. 3 (b) shows the Be atomic concentration as a function of Be effusion cell temperature inferred from the SIMS measurements.

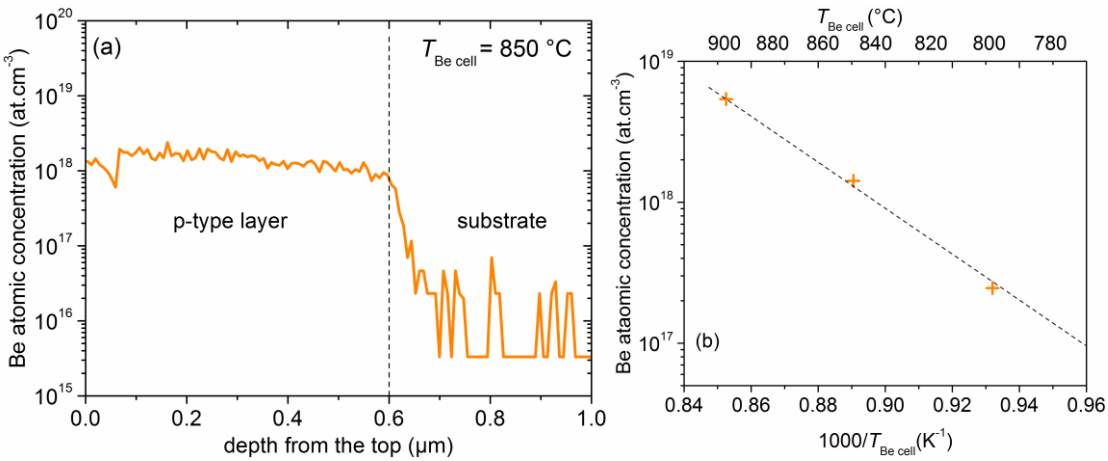

FIG. 3: (a) SIMS profile measurement for a Be effusion cell temperature equal to 850°C. (b) Be atomic concentration as a function of Be effusion cell temperature (the dashed line is a guide for the eye).

Owing to the small bandgap of InSb, we assumed that the Be activation coefficient (ratio of free holes to atomic Be concentrations) is equal to one. Consequently, the Be cell temperature required to reach a doping concentration (N_a) of 10^{17}cm^{-3} in the p-type top layer was found to be 770°C.

II.2. TECHNOLOGICAL PROCESSES

The InSb photovoltaic cells with optimized doping levels in the structure grown by MBE were processed with a standard UV photolithography technique using AZ5214 photoresist to define circular mesa devices with diameters of 210 µm, 130 µm, 90 µm and 70 µm. The mesa etching was performed with a 50:1 ratio of citric acid and hydrogen peroxide solution at room temperature [31]. The resulting depth of the mesa is approximately 1.8 µm. Thus the bottom of the mesa is located close to the middle of the n-doped InSb layer (1.75 µm from the top surface) grown by MBE. Figure 4 depicts a schematic illustration of a cross-section of the PV cell, a SEM image of the side wall of the mesa structure and a top view of a PV cell obtained by optical microscopy. In this first generation of InSb PV cells for near-field thermophotovoltaics, it was chosen not to add any anti-reflection coating. Given the microscopic size of the mesas,

the cells were passivated just after mesa etching to prevent parallel current surface leakages that manifest in the dark current-voltage characteristics (in particular in reverse bias). Actually, especially in the case of low-bandgap materials - which are almost metals -, side walls of the mesa provide a conductive channel for the electrical charges. Different passivation techniques contribute to avoid accumulation of majority carriers at these side walls and thus to increase the cell performances [32]. After various tests using different materials, an organic passivation technique [33] was selected with using the AZ1518 photoresist. This photoresist was spin coated with a speed of 4000 rpm, and the resulting 1.8 µm-thick layer was baked at 200 °C for 2 hours in an oven [34]. Finally, 20 nm/20 nm/200 nm of Ti/Pt/Au ohmic contacts were added using e-beam evaporation on the top of the p-type mesa and 20 nm/200 nm of Ti/Au contacts at the back of the n-type substrate. In the end, to the circular mesa diameters of 210 µm, 130 µm, 90 µm and 70 µm, correspond diameters of the active (uncovered) areas of 160 µm, 80 µm, 40 µm and 20 µm, respectively.

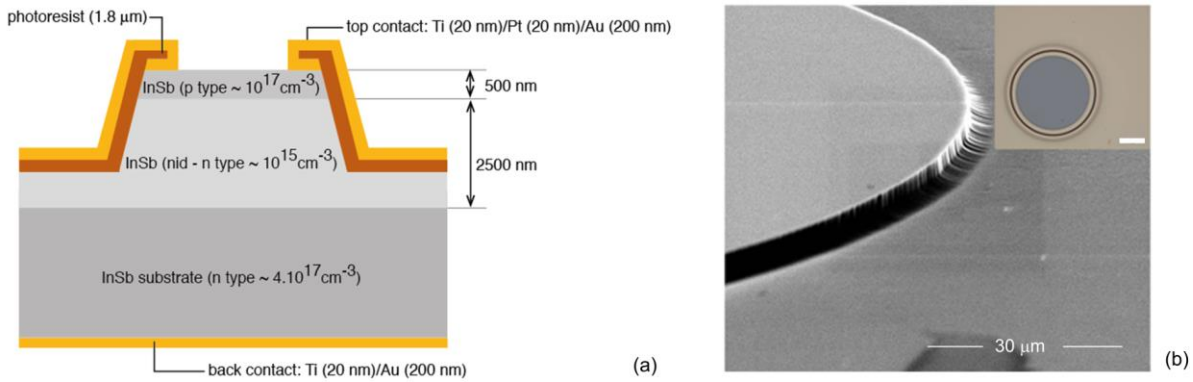

FIG. 4: (a) Schematic of the PV cell structure. (b) SEM image of the side wall of the mesa. Inset: top-view optical image of the PV device.

III. ELECTRICAL CHARACTERIZATIONS

For characterizing the electrical performances of the fabricated PV cells, current-voltage (I-V) characteristics were measured using a Keithley 2400 source meter in an ARS 4K probe station. Temperature of the cell was controlled by means of a cryostat and could be regulated from 77 K to 197 K. During measurements of the dark current density-voltage (J_d-V) curves, in order to prevent radiation coming from the environment at 300 K to illuminate the cell, a top nickel-plated shield inserted in the probe station was used. During measurements of the I-V curves under illumination, an IR-12K infrared (IR) radiation source having a 3.5 mm x 3.5 mm active area was mounted 4 cm above the sapphire windows of the probe station without using

any focusing optics. The distance between the emitting surface of the IR source and the cell was 9.5 cm. The fraction coming from the IR source can be calculated knowing the area of the source, the active area of the cell, the distance separating them (view factor), the source temperature, and the spectral optical properties of the IR source (SiC) and of the two windows of the probe station (sapphire). In the case with the largest temperature of the IR source (1248 K) and the largest mesa diameter (210 μm), this contribution is approximately 0.44 μW. In addition, radiation power coming from the surroundings (within and outside the probe station) has to be taken into account. It can be much larger. For example, the same cell subject to a hemispherical background radiation at 20 °C would receive an additional power of roughly 8.4 μW. The probe station allows neither the full elimination nor an accurate estimation of that contribution to the incident power. Therefore, conversion efficiency cannot be assessed for these cells. Report on their electrical properties will be made as a function of mesa size, operating temperature and illumination conditions.

III.1. DARK J-V CURVES

Figure 5 (a) shows the dark current density-voltage (J_d-V) curves (semi-log scale plot, absolute values) of InSb PV cells having different mesa diameters. For all J_d-V curves, the current in reverse bias is always smaller than 10^{-4} A cm^{-2}. In addition, it is important to notice that the J_d-V curves do not depend much on the size of the mesa, proving that passivation with photoresist is performing well. It is worth noticing that the minimum of the J_d-V curves is not located at $V = 0$. This indicates that despite the shielding, a slight photonic current due to the thermal radiation of the probe station and its surroundings is measured. This means that these curves are not perfect dark current density-voltage characteristics, as clearly shown in Fig. 5 (b) (linear scale plot). If the curves are vertically shifted so that they all cross at the origin, they superimpose (not shown). This suggests that cells performances in the dark barely depend on the mesa size. However, by using the mesa area to calculate current densities, one finds that the larger the cell, the better its performances.

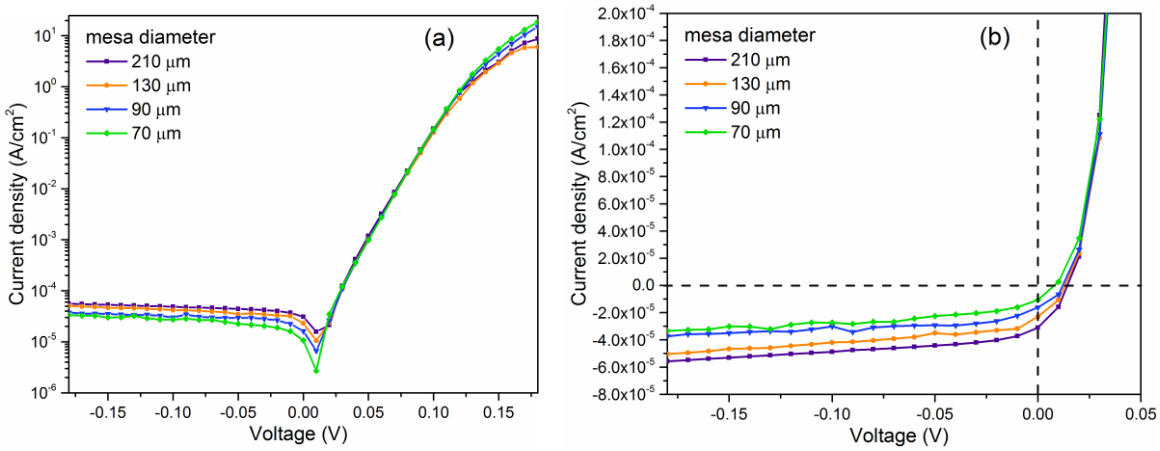

FIG. 5. Dark J-V curves of InSb PV cells at 77 K having different mesa sizes and passivated with photoresist: (a) semi-log scale and (b) linear scale plots.

The J_d-V curves of an InSb PV cell having a mesa diameter of 210 μm and passivated with photoresist were measured as a function of temperature, from 77 K up to 197 K (Fig. 6). For the lowest two temperatures (77 K and 97 K), a small current caused by the background thermal radiation can be observed, which demonstrates the high sensitivity of the device. When temperature of the cell increases, the dark current in both reverse and forward bias conditions raises by large factors. The background thermal radiation is not visible anymore (the minimum is at $V = 0$, *i.e.* the dark current dominates). This result confirms that a near-field thermophotovoltaic device with an InSb PV cell operating at 300 K, theoretically investigated multiple times [12, 18, 35-42], is clearly impracticable.

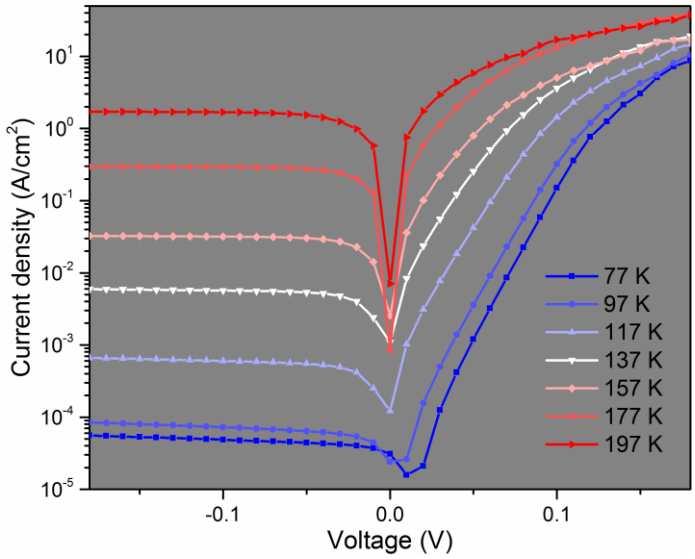

FIG. 6. Dark J-V curves of InSb PV cells having a mesa diameter of 210 μm and passivated with photoresist, as a function of temperature.

III.2. I-V CURVES UNDER ILLUMINATION

After measurements of current-voltage characteristics in the dark, performances of the InSb cells under illumination were investigated. First, Fig. 7 (a) shows that when the top nickel-plated shield is removed, the sole illumination of the background at room temperature (300 K) is able to generate a photovoltaic power in InSb cells at 77 K. The current-voltage characteristic curves under illumination exhibit a short-circuit current of the order of nA and open-circuit voltages reaching up to 70 mV. Note that these curves are often in the fourth quadrant, but here the sign of the current was changed in order to observe the IV curves in the first quadrant. Consistently with results shown in Fig. 5 (b), where a photovoltaic effect is visible due to a residual background illumination, the performances of the cell (open-circuit voltage) increase with the mesa size. Then the level of illumination provided by the infrared (IR) radiation source was varied, by changing its setting temperature at three values (948 K, 1098 K, and 1248 K, using a calibration curve from the IR-12K manufacturer). Figure 7 (b) shows the corresponding I-V curves for InSb cells at 77 K having a mesa diameter of 210 μm. As expected, the I-V curves shift farther up right into the first quadrant as the IR source temperature is increased. Indeed more radiation is collected, hence both the short-circuit current and the open-circuit voltage increase because of more photocarrier generation in the cell. Under the largest illumination level (setting temperature of the IR source equal to 1248 K), the open-circuit voltage is equal to around 83 mV, the short-circuit current is about 10 μA, the electrical power at the maximum power point is 0.531 μW and the corresponding fill factor is 0.64 (consistent with the fact that the I-V curve is not a straight line). The large fill factor value can be attributed to the micron size of the cell, large mobility of holes in the p-doped layer (~ 2000 $cm^2\ V^{-1}\ s^{-1}$ at 77 K) and high-quality contacts.

In the upcoming step (3) of developing a laboratory NF-TPV demonstrator, these indium antimonide PV cells will be operated with a thermal source in the near field. Simulations of illumination conditions predict levels higher than the largest one investigated in the present article. Hence it is ensured that these photovoltaic cells will be suitable for measuring a near-field enhancement of the generated electrical power. Future consideration of using more complex structures than p-n junctions, for example by adding a window layer, requires keeping in mind the constraints of near-field illumination and metamorphic growth.

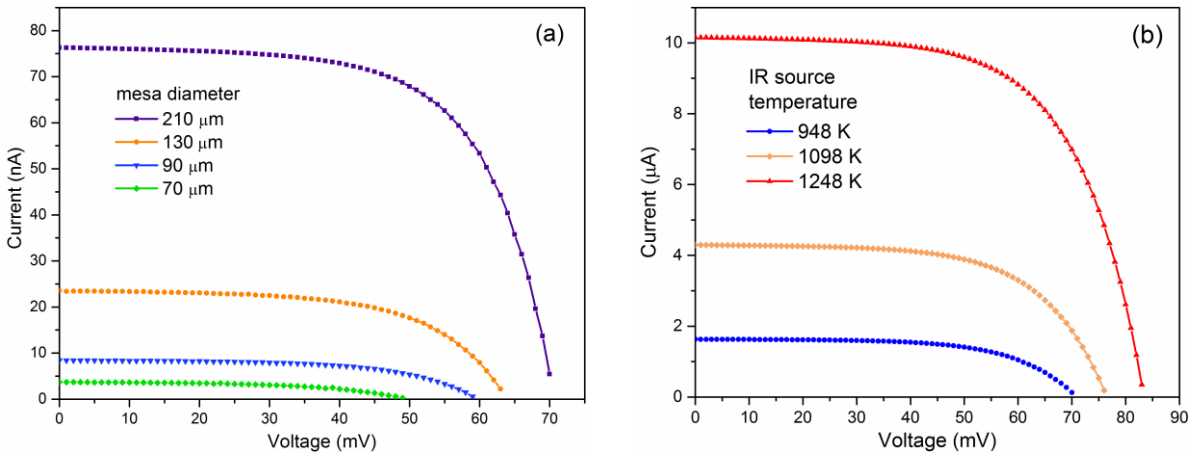

FIG. 7: Electrical performances of InSb PV cells passivated with photoresist at 77 K, (a) having different mesa diameters illuminated by the background radiation at 300 K, (b) having a mesa diameter of 210 μm (active area diameter of 160 μm) under illumination by the IR source with various source temperatures.

IV. CONCLUSIONS

Based on a prior design, micron-sized indium antimonide photovoltaic cells have been fabricated and characterized. The optimum conditions for deoxidation of the substrate, MBE growth with the incorporation of dopants of n-doped and p-doped layers have been determined. Characterization by X-ray diffraction, photoluminescence, and atomic force microscopy have demonstrated the high quality of the resulting p-n junction diode layers grown on a n-doped substrate. The processing steps of micron-sized circular mesa structures have been described in detail. Performances of the resulting photovoltaic cells have been measured without and with an external infrared radiation source, as a function of the diameter of the mesa, the operating temperature of the cell, and under various illumination conditions. A striking result is that even under illumination by the background at room temperature, well-resolved diode-like current-voltage characteristics have been observed, with open-circuit voltages reaching up to 70 mV. Under far-field illumination by an infrared radiation source, a single cell has exhibited even larger open-circuit voltages, short-circuit currents of several microamps and an electrical power at the maximum power point reaching more than 0.5 μW in the best case. Room-temperature background generates thermophotovoltaic power, thus it can be anticipated that near-field thermal radiation-to-electricity conversion will be efficient with these cells, even if the thermal source is moderately hot.

ACKNOWLEDGEMENTS

Financial support by the French National Research Agency (ANR) under grant No. ANR-16-CE05-0013 and partial funding by the French "Investment for the Future" program (EquipEx EXTRA, ANR-11-EQPX-0016) and by the Occitanie region are acknowledged.

REFERENCES

1. T. Bauer, Thermophotovoltaics: basic principles and critical aspects of system design, Springer Science & Business Media, 2011.

2. D. Chubb, Fundamentals of thermophotovoltaic energy conversion, Elsevier, 2007.

3. J.L. Pan, H. K. Choy, C. Fonstad, Very large radiative transfer over small distances from a black body for thermophotovoltaic applications, IEEE Trans. Electron Dev. 47 (2000) 241-249.

4. M. Whale, E.G. Cravalho, Modeling and performance of microscale thermophotovoltaic energy conversion devices, IEEE Trans. Energy Convers. 17 (2002) 130-142.

5. A. Narayanaswamy, G. Chen, Surface modes for near field thermophotovoltaics, Appl. Phys. Lett. 82 (2003) 3544-3546.

6. M. Laroche, R. Carminati, J.-J. Greffet, Near-field thermophotovoltaic energy conversion, J. Appl. Phys. 100 (2006) 063704.

7. A. Fiorino, L. Zhu, D. Thompson, R. Mittapally, P. Reddy, E. Meyhofer, Nanogap near-field thermophotovoltaics, Nat. Nanotechnol. **13** (2018) 806.

8. K. Park, S. Basu, W. King, Z. Zhang, Performance analysis of near-field thermophotovoltaic devices considering absorption distribution, J. Quant. Spectrosc. Radiat. Transf. 109 (2008) 305-316.

9. M. Francoeur, R. Vaillon, M.P. Mengüç, Thermal impacts on the performance of nanoscale-gap thermophotovoltaic power generators, IEEE Trans. Energy Convers. 26 (2011) 686-698.

10. T. Bright, L. Wang, Z. Zhang, Performance of near-field thermophotovoltaic cells enhanced with a backside reflector, J. Heat Transf. 136 (2014) 062701.

11. M. P. Bernardi, O. Dupré, E. Blandre, P.-O. Chapuis, R. Vaillon, M. Francoeur, Impacts of propagating, frustrated and surface modes on radiative, electrical and thermal losses in nanoscale-gap thermophotovoltaic power generators, Sci. Reports 5 (2015) 11626.

12. M. Lim, S. Jin, S.S. Lee, B.J. Lee, Graphene-assisted Si-InSb thermophotovoltaic system for low temperature applications, Opt. Express 23 (2015) A240-A253.

13. S. Jin, M. Lim, S.S. Lee, B.J. Lee, Hyperbolic metamaterial-based near-field thermophotovoltaic system for hundreds of nanometer vacuum gap, Opt. express 24 (2016) A635-A649.
14. J.Z.-J. Lau, V.N.-S. Bong, B.T. Wong, Parametric investigation of nano-gap thermophotovoltaic energy conversion, J. Quant. Spectrosc. Radiat. Transf. **171** (2016) 39-49.
15. E. Blandre, P.-O. Chapuis, R. Vaillon, High-injection effects in near-field thermophotovoltaic devices, Sci. Reports 7 (2017) 15860.
16. M. Elzouka, S. Ndao, Towards a near-field concentrated solar thermophotovoltaic microsystem: Part I–Modeling**,** Sol. Energy 141 (2017) 323-333.
17. J.Z.-J. Lau, B.T. Wong, Thermal energy conversion using near-field thermophotovoltaic device composed of a thin-film tungsten radiator and a thin-film silicon cell, J. Appl. Phys. 122 (2017) 084302.
18. M. Lim, S.S. Lee, B.J. Lee, Effects of multilayered graphene on the performance of near-field thermophotovoltaic system at longer vacuum gap distances, J. Quant. Spectrosc. Radiat. Transf. 197 (2017) 84-94.
19. N. Vongsoasup, M. Francoeur, K. Hanamura, Performance analysis of near-field thermophotovoltaic system with 2D grating tungsten radiator, Int. J. Heat Mass Transf. 115 (2017) 326-332.
20. Y. Yang, J.-Y. Chang, P. Sabbaghi, L. Wang, Performance analysis of a near-field thermophotovoltaic device with a metallodielectric selective emitter and electrical contacts for the photovoltaic cell, J. Heat Transf. 139 (2017) 052701.
21. M. Lim, J. Song, J. Kim, S.S. Lee, I. Lee, B.J. Lee, Optimization of a near-field thermophotovoltaic system operating at low temperature and large vacuum gap, J. Quant. Spectrosc. Radiat. Transf. 210 (2018) 35-43.
22. J. Song, M. Lim, S.S. Lee, B. J. Lee, Analysis of photocurrent generation within a Schottky-junction-basedn-field thermophotovoltaic system, Phys. Rev. Applied 11 (2019) 044040.
23. R. Vaillon, J.P. Pérez, C. Lucchesi, D. Cakiroglu, P.O. Chapuis, T. Taliercio, E. Tournié, Micron-sized liquid nitrogen-cooled indium antimonide photovoltaic cell for near-field thermophotovoltaics, Opt. Express 27 (2019) A11-A24.
24. A. Datas, R. Vaillon, Thermionic-enhanced near-field thermophotovoltaics, Nano Energy 61 (2019) 10-17.
25. A. Datas, R. Vaillon, Thermionic-enhanced near-field thermophotovoltaics for medium-grade heat sources, App. Phys. Letters 114 (2019) 133501.

26. R. St-Gelais, L. Zhu, S. Fan, M. Lipson, Near-field radiative heat transfer between parallel structures in the deep subwavelength regime, Nat. Nanotechnol. 11 (2016) 515.
27. W. Huang, L. Lei, L. Li, J.A. Massengale, R.Q. Yang, T.D. Mishima, M.B. Santos, Enhanced collection efficiencies and performance of interband cascade structures for narrow bandgap semiconductor thermophotovoltaic devices, J. Appl. Phys. 124 (2018) 023101.
28. I. Shtrichman, D. Aronov, M. Ben Ezra, I. Barkai, E. Berkowicz, M. Brumer, R. Fraenkel, A. Glozman, S. Grossman, E. Jacobsohn, O. Klin, P. Klipstein, I. Lukomsky, L. Shkedy, N. Snapi, M. Yassen, E. Weiss E., High operating temperature epi-InSb and XBn-InAsSb photodetectors, Infrared Technology and Applications XXXVIII, 8353 (2012) 83532Y.
29. W.K. Liu, M.B. Santos, Surface reconstructions of InSb (001) during molecular beam epitaxy, Surf. Sc. 319 (1994) 172-183.
30. R. Tessler, C. Saguy, O. Klin, S. Greenberg, E. Weiss, R. Akhvlediani, R. Edrei, A. Hoffman, Desorption of InSb (001) native oxide and surface smoothing induced by low temperature annealing under molecular hydrogen flow, J. Appl. Phys 101 (2007) 024513.
31. K.M. Chang, J.J. Luo, C.D. Chiang, K.C. Liu, Wet etching characterization of InSb for thermal imaging applications, Jap. J. Appl. Phys. 45 (2006) 3A.
32. P. Y. Delaunay, A. Hood, B. M. Nguyen, D. Hoffman, Y. Wei, M. Razeghi, Passivation of type-II InAs⁄GaSb double heterostructure, Appl. Phys. Letters 91 (2007) 091112.
33. E. A. Plis, M. N. Kutty, and S. Krishna, Passivation techniques for InAs/GaSb strained layer superlattice detectors, Laser Photonics Rev. 7 (2013) 45-59.
34. R. Chaghi, C. Cervera, H. Ait-Kaci, J.B. Rodriguez, P. Christol, Wet etching and chemical polishing of InAs/GaSb superlattice photodiodes, Semicond. Sci. Technol. 24 (2009) 065010.
35. O. Ilic, M. Jablan, J.D. Joannopoulos, I. Celanovic, M. Soljačić, Overcoming the black body limit in plasmonic and graphene near-field thermophotovoltaic systems, Opt. Express 20 (2012) A366-A384.
36. R. Messina, P. Ben-Abdallah, Graphene-based photovoltaic cells for near-field thermal energy conversion, Sci. Reports 3 (2013) 1383.
37. V. Svetovoy, G. Palasantzas, Graphene-on-silicon near-field thermophotovoltaic cell, Phys. Rev. Appl. 2 (2014) 034006.
38. A. Karalis, J. Joannopoulos, Temporal coupled-mode theory model for resonant near-field thermophotovoltaics, Appl. Phys. Lett. 107 (2015) 141108.
39. A. Karalis, J. Joannopoulos, 'Squeezing'near-field thermal emission for ultra-efficient high-power thermophotovoltaic conversion, Sci. Reports 6 (2016) 28472.

40. M. Mirmoosa, M. Omelyanovich, C. Simovski, Microgap thermophotovoltaic systems with low emission temperature and high electric output, J. Opt. 18 (2016) 115104.
41. T. Liao, Z. Yang, W. Peng, X. Chen, J. Chen, Parametric characteristics and optimum criteria of a near-field solar thermophotovoltaic system at the maximum efficiency, Energy Convers. Manag. 152 (2017) 214-220.
42. T. Liao, Z. Yang, Q. Dong, X. Chen, J. Chen, Performance Evaluation and Parametric Optimum Choice Criteria of a Near-Field Thermophotovoltaic Cell, IEEE Transactions on Electron Devices 64 (2017) 4144-4148.